

The spatial and velocity structure of circumstellar water masers

F. Colomer¹, M.J. Reid², K.M. Menten³, and V. Bujarrabal¹

¹ Observatorio Astronómico Nacional (IGN), Apartado 1143, 28800 Alcalá de Henares, Spain

² Harvard-Smithsonian Center for Astrophysics, MS-42, 60 Garden Street, Cambridge, MA 02138, USA

³ Max-Planck-Institut für Radioastronomie, Auf dem Hügel 69, 53121 Bonn, Germany

Received 23 April 1999 / Accepted 13 December 1999

Abstract. We report observations with the VLA of 22 GHz H₂O maser emission in the circumstellar envelopes of 11 late-type stars. We model the maser emission towards six of them (IRC +60169, R Crb, U Her, RX Boo, RLMi, and R Cas) with a computer program we have developed, that fits three-dimensional Gaussian sources (in position and velocity) to the measured intensity distribution. This approach to the problem is superior to the standard procedure of fitting two-dimensional Gaussian models to images for each frequency channel, and it is shown to be a powerful method of identifying blended and/or weak maser features.

As a result, we find that the H₂O maser emission is located in a thin shell expanding from the star in four cases, despite of the fact that the emission is clumpy and the shells appear incomplete. Moreover, our maps indicate that the H₂O maser emission comes from inner parts of the circumstellar envelope, which are comparable in extent to the regions in which dust grains form and in which the expanding envelope has not reached its terminal velocity.

Our analysis also provides the spectral linewidth of each maser feature, which contains information about the physical conditions in the emitting region. In particular, it provides a tool to discriminate whether or not these masers are saturated as, for unsaturated masers, theory predicts that a correlation between the strongest features and the narrowest linewidths should exist. This behaviour is found in at least U Her, RX Boo, and R Cas.

Key words: masers – techniques: interferometric – stars: circumstellar matter – stars: late-type

1. Introduction

Interstellar and circumstellar maser emission from the water molecule has been detected in a large number of objects (cataloged by Cesaroni et al. 1988; Brand et al. 1994). The most extensively studied H₂O masers are the $6_{16} \rightarrow 5_{23}$ transitions at $\lambda = 1.35$ cm (22 GHz), frequently found in the circumstellar envelopes produced by mass loss from evolved stars. Early VLBI observations were done by Spencer et al. (1979); many later studies have used the Very Large Array (VLA) in A con-

figuration (e.g. Johnston et al. 1985). Other H₂O maser lines down to submillimeter wavelengths have been also detected (e.g. Menten & Young 1995).

Chapman & Cohen (1986) concluded from their study of the supergiant VX Sgr that the SiO, H₂O, and OH masers form a natural sequence at increasing radii from the star. Several authors have found that, in a few objects, the H₂O maser emission is consistent with the expanding shell models (Spencer et al. 1979; Lane et al. 1987 on IK Tau; Diamond et al. 1987). This was also reported by Reid & Menten (1990), who were able to detect as well the photosphere of W Hya, providing the stellar radius and, for the first time, could locate the circumstellar maser emission with respect to the central star. Nevertheless, in other objects there is evidence of non-spherical geometric distributions, where the standard expanding shell model fails to fit the H₂O maser data (Johnston et al. 1985; Lane et al. 1987; Bowers et al. 1993; Bowers & Johnston 1994; Yates & Cohen 1994). Careful mapping of the position and velocity of the individual maser features is necessary to illuminate this point, and new approaches of data analysis are needed particularly for studies with instruments of moderate angular resolution like the VLA.

It is also important to know whether the extent of the masing region increases with mass-loss rate, as this is predicted by model pumping calculations (Cooke & Elitzur 1985). Water maser regions have been reported to show sizes in the range 10^{14} cm (or 6 AU; Spencer et al. 1979) to more than 10^{16} cm (~ 1000 AU; Johnston et al. 1985; Yates & Cohen 1994). Lane et al. (1987) find that H₂O masers in Mira-type stars are produced within regions of diameter 9 - 108 AU, while for supergiant stars maser shell diameters of 300 - 720 AU are observed. These results are consistent with those of Bowers et al. (1993). An empirical correlation between H₂O maser region size and mass-loss rate has been found by Lane et al. (1987) and Yates & Cohen (1994).

Most of the mentioned studies, however cannot provide information on the sizes of individual spots due to lack of angular resolution (the VLA is unable to resolve the spots, as its minimum fringe spacing is $0''.07$). Spots were reported to be of the order of 10^{13} cm from VLBI data (Spencer et al. 1979; Diamond et al. 1987); however recent VLBI observations estimate that compact structures almost an order of magnitude smaller (e.g. $\sim 3 \cdot 10^{12}$ cm; Imai et al. 1997) exist.

Send offprint requests to: Francisco Colomer (colomer@oan.es; <http://www.oan.es/>)

An interesting problem that remains to be solved is to establish where the H₂O masers appear in the expanding circumstellar envelope. The existing data suggest that the distance from the star at which these masers arise is smaller than the distance at which dust is formed (measured by infrared interferometers, or by the thermal emission of SiO). This can be explained if the density is large enough inside the dust formation point, and it is compatible with the moderate velocities seen in these masers.

2. Observations

The observations were performed on 1990 June 2 and 3, with 25 antennas of the Very Large Array¹ (VLA) in A configuration, providing a minimum fringe spacing of 0''07 at the frequency of the $J = 6_{16} \rightarrow 5_{23}$ maser transition of the water molecule (rest frequency 22235.080 MHz). A total of 11 late-type stars were observed in snapshot mode (one or more scans per source of 4.5 minutes duration), together with continuum calibration sources. Good u-v coverage was obtained for all sources despite of the short duration of the observations thanks to the VLA 300 instantaneous baselines. The VLA correlator setup provided 127 spectral channels cross-correlation spectra every 30 seconds. The total bandwidth covered was 3.125 MHz (or 42.2 km s⁻¹), resulting in a spectral resolution of 0.33 km s⁻¹.

3. Data analysis

We have used the NRAO Astronomical Image Processing System (AIPS) in every step of the data reduction procedure. Absolute amplitude calibration was attained by observing the quasar 0501 – 019 (with total flux assumed to be 3.36 Jy from a previous experiment) over a wide range of elevations. The calibration solutions (amplitude and phase) were applied to the H₂O maser sources. A spectral channel with good signal-to-noise ratio (SNR) displaying little or no amplitude variation with changing baseline length (so, likely to be unresolved and isolated) was selected to be used as a phase-reference for each source. Self-calibration techniques, coded into AIPS, were used to obtain complex gain corrections.

We produced maps of the H₂O maser data, and processed them with the 3D Gaussian fitting computer program “FG3” (see the appendix at the end of this paper). This program has been developed for the inspection and analysis of spectral line data cubes. The obtained CLEAN components were inspected, and the initial guesses for “FG3” were checked against them.

We have used our 3D Gaussian fitting program to search for the sources responsible for the H₂O maser emission in the envelopes of these late-type stars. The fitted position errors $\sigma_{\alpha,\delta}$ are in agreement with the statistical prediction of those errors based on the SNR,

$$\sigma_{\alpha,\delta} \simeq \frac{\beta T_{\text{sys}}}{\sqrt{\Delta\nu \tau N(N-1)}} \frac{\theta_{\alpha,\delta}}{2} \frac{1}{I} \quad , \quad (1)$$

¹ The National Radio Astronomy Observatory is operated by Associated Universities, Inc., under cooperative agreement with the National Science Foundation.

where $\theta_{\alpha,\delta}$ represents the synthesized beam (FWHM) in right ascension or declination, respectively, $\beta \simeq 1.5$ is a digital processing factor, T_{sys} is the geometric mean of the antenna system temperatures in Janskys, N is the number of participating telescopes, τ the integration time, $\Delta\nu$ the channel bandwidth, and I the fitted Gaussian flux. The cumulative reduced χ^2 value for all the Gaussian fits was close to unity, confirming the consistency of the Gaussian fitting procedure, that had been already tested on VX Sgr by Greenhill et al. (1995).

4. Results for the individual sources

We will discuss the results obtained for 6 late-type stars, selected among our sample of sources because the other ones turned out to be too weak or appeared unresolved (see Sect. 4.7). The spatial distribution of H₂O maser emission has been modelled as a shell around the central star for 5 of them, whose characteristics are listed in Table 1. The distances to these sources have been derived from the Period-Luminosity relation of Feast et al. (1989), using the K-magnitude values in Gezari et al. (1987). This procedure has been demonstrated to be precise by Reid & Menten (1997). Mass-loss rates have been calculated using the method and CO intensities in Loup et al. (1993), rescaling their values to the adopted distances.

4.1. R Crt

The star R Crt is known to show maser emission by the SiO, H₂O, and OH molecules. Being a semi-regular variable, it is not clear what its intrinsic luminosity is, and its distance can only be crudely estimated. We assume R Crt is an overtone pulsator, and adopt a distance of 186 pc in our discussion.

Given the complex frequency spectrum of R Crt (see Fig. 1), it was not easy to choose a good frequency channel to be used as phase-reference. We selected the intensity peak at 16.86 km s⁻¹ and extracted it from the database, proceeding to self-calibrate this emission as described above. The resulting u-v database was CLEANed and mapped, producing a 128x128 pixels map with 0''01x0''01 pixel spacing. A Gaussian beam of 0''135x0''095 HPBW at a position angle of 22° was obtained for uniform weighting. The whole database was mapped using a circular restoring beam of 0''10 HPBW. Only channels in the velocity range of 2.4 to 20.1 km s⁻¹ had emission. Then, we used the 3D Gaussian fitting program to find true maser components. The results are listed in Table 2, and the equivalent map is shown in Fig. 2. The area of the circles is proportional to the spot intensity. The individual maser features are spatially unresolved in our observations.

The terminal velocity of the R Crt envelope is estimated to be 11 km s⁻¹ from CO observations by Zuckerman & Dyck (1986). The CO radius is 5.6 10¹⁶ cm, and the star has a mass-loss rate of 5.5 10⁻⁷ M_⊙/yr (rescaling the values in Loup et al. 1993 to the adopted distance). Dickinson et al. (1986) studied the OH maser emission, which shows components at about 10 km s⁻¹ (the stellar velocity), as well as intense blue emission around 2 km s⁻¹, and red emission in the range 16– 22 km s⁻¹, which

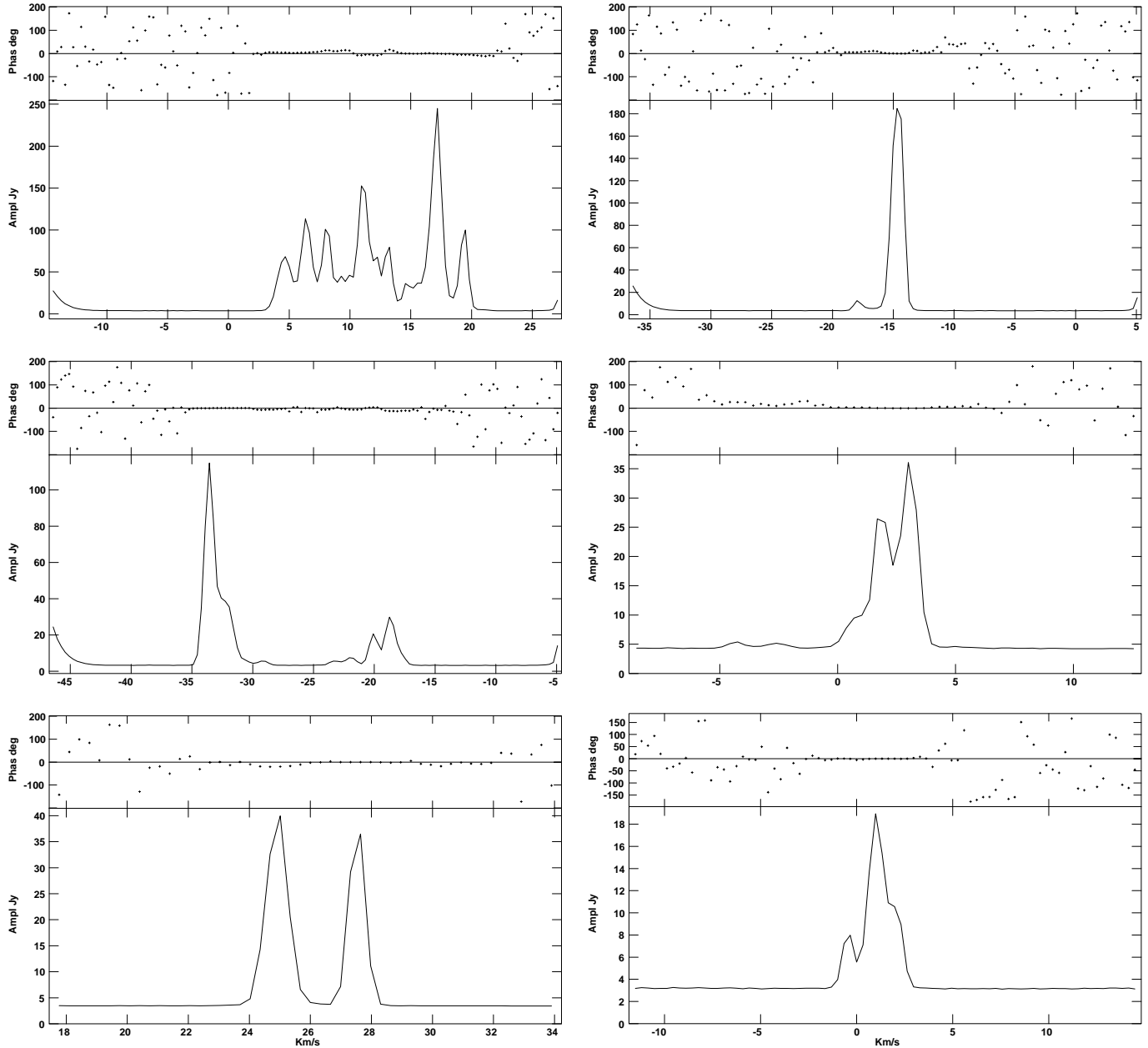


Fig. 1. Averaged cross-spectrum of the H₂O maser emission, respectively, in R Crb, U Her, IRC +60169, RX Boo, R Cas, and RLMi (from left to right, and top to bottom).

suggests an expansion velocity of $\sim 10 \text{ km s}^{-1}$. The overall distribution of H₂O maser emission shown by Bowers & Johnston (1994), indicating a complex T-shaped morphology, is similar to ours, shown in Fig. 2. We have tried to fit the H₂O maser spot velocities versus distance to the centroid of emission, at $(-0''.023, -0''.065)$ (very close to the midpoint between the lowest velocity feature, at 3.8 km s^{-1} , and the highest velocity feature, at 19.1 km s^{-1}), assuming a systemic velocity of 10.8 km s^{-1} , and an expansion velocity of 8 km s^{-1} . We have found a solution for a shell radius of $0''.082$, or $\sim 2.3 \cdot 10^{14} \text{ cm}$ at a distance of 186 pc.

The relation between the intensity fitted for each maser feature and its linewidth is shown in Fig. 3. We discuss in Sect. 5.2

the implications of this correlation, that helps to discriminate if the masers are saturated. However, for R Crb it is not possible to draw any strong conclusions from Fig. 3.

4.2. U Her

The results for the Mira-type star U Her, whose spectrum is shown in Fig. 1, are displayed in Figs. 4 and 5. We find both similarities and differences between our results and those of Bowers & Johnston (1994). We find the H₂O maser features spread in velocity along 9.5 km s^{-1} , in contrast to their wider 16.8 km s^{-1} band. However, some of the strongest spectral features they observed appear at velocities where we also see emission (Fig. 1).

Table 1. Characteristics of the H₂O maser sources discussed in Sect. 4

Source	IRC +60169	R Crt	RX Boo	U Her	R Cas
α (2000.0)	06 34 34.88	11 00 34.01	14 24 11.58	16 25 47.60	23 58 24.40
δ (2000.0)	60 56 33.19	-18 19 29.29	25 42 16.03	18 53 33.00	51 23 18.00
v_{LSR}	-20	10.8	1	-15	24
v_{bandpass}	-26	6	3	-16	26
Spectral type	M8.5	M7	M6.5e–M8IIIe	M5e–M8e	M6e–M10e
Var. type	OH/IR	SRb	SRb	M	M
$^a P$	–	160	340:	405	430
$^b M_k$	–	-6.38	-7.77	-8.04	-8.13
$^c m_k$	–	-1.3	-2.0	-0.3	-1.8
$^d D$	690	186	141	347	184
$^e \dot{M}$	4.90	0.55	0.56	0.52	1.01
$^f v_{\text{terminal}}$	19.7	11	10	6	12
g Masers	SHO	SHO	SH	SHO	SHO

^a Period of the variable star in days.

^b K-magnitude as obtained from the P-L relation of Feast et al. (1989).

^c Apparent K-magnitude, from Gezari et al. (1987).

^d Distance in parsec, calculated from the definition $m_k - M_k = 5 \log D - 5$, except for IRC +60169 (see details in Sect. 4).

^e Mass loss rate in $10^{-6} M_{\odot}/\text{yr}$. Rescaled from Loup et al. (1993), assuming the source distances quoted D .

^f Terminal velocity, in km s^{-1} .

^g Molecules with detected maser emission (SiO coded as “S”, H₂O as “H”, and OH as “O”).

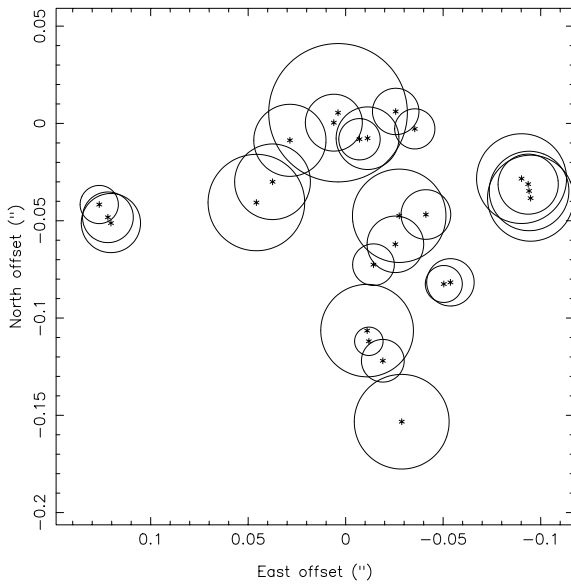


Fig. 2. Results of the 3D Gaussian fitting program “FG3” for the H₂O masers in R Crt. See Table 2 for the spot velocity.

They place the central star position at the midpoint between the lowest and highest velocity emission, finding a shell structure characterized by an asymmetric emission loop to the south. In contrast, our results provide a much smaller number of features, which reproduce quite well the overall distribution (see Table 3). Fig. 4 shows that the H₂O maser spots in U Her are distributed in a ring. We may try to fit a shell structure, choosing the star position at $(-0''.05, +0''.05)$, near the center of the distribution. However, we find no simple solution to the fit. A thick shell of inner radius of 45 mas ($2.3 \cdot 10^{14}$ cm for a distance of 347 pc) and

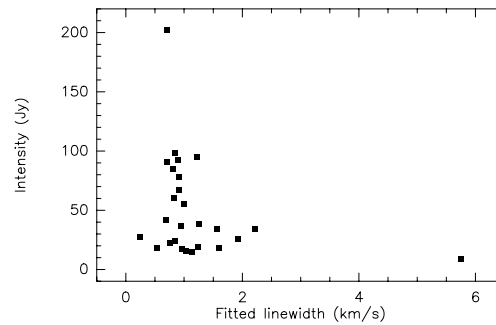


Fig. 3. Fitted maser linewidth versus fitted intensity, for R Crt.

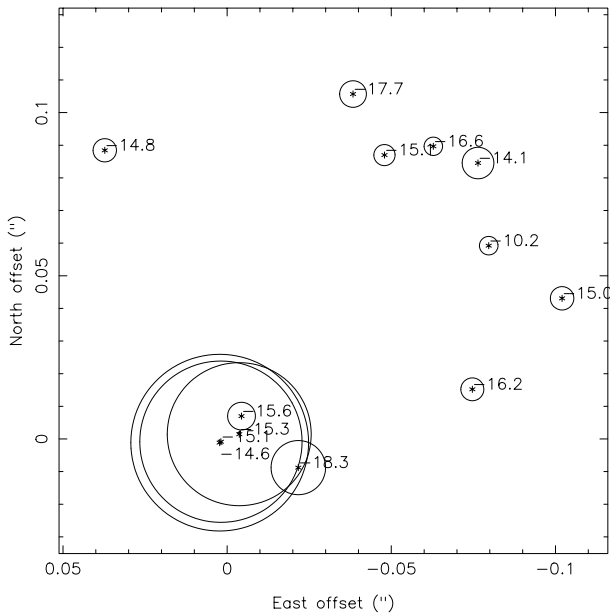
outer radius of 70 mas ($3.6 \cdot 10^{14}$ cm) might be compatible with our data, using an expansion velocity of $\sim 6 \text{ km s}^{-1}$. Such a size is also compatible with the map in Fig. 4, and is much smaller than the CO radius of $\sim 4.9 \cdot 10^{16}$ cm obtained by rescaling the value in Loup et al. (1993) to the distance of 347 pc.

4.3. IRC +60169

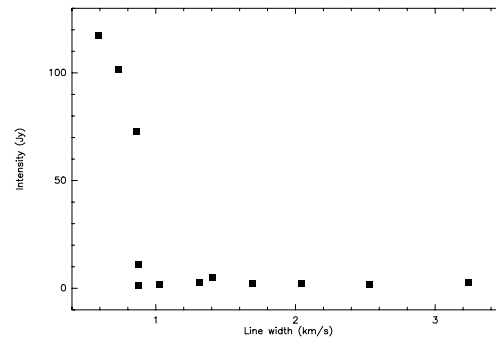
Figs. 6, 7, and Table 4, show the results for the supergiant star IRC +60169. The processing of the IRC +60169 data cube with the 3D Gaussian fitting program “FG3” yielded very interesting results. The spectrum of the H₂O masers in IRC +60169 (Fig. 1) shows the existence of at least two groups of features. The features around -31 to -36 km s^{-1} , the most blue-shifted, coincide in velocity with the blue peak in the OH spectrum obtained by Slootmaker et al. (1985). The features around the velocity of the star, -23 km s^{-1} (the center of the OH and SiO spectra), are distributed in a ring-like structure around the blue peak. We find that such a H₂O maser distribution can be fitted by a spherical

Table 2. Fitted H₂O maser features in R Cr. Uncertain features are marked with an asterisk, as explained in Sect. A.4

V _{LSR}	σ _{V_{LSR}}	I (Jy)	σ _I	Δα('')	σ _{Δα}	Δδ('')	σ _{Δδ}	Δv	σ _{Δv}
3.782	0.014	17.0	0.34	-0.035	0.0007	-0.003	0.0009	0.957	0.019
4.290	0.003	19.3	0.30	-0.019	0.0004	-0.122	0.0011	1.241	0.010
4.321	0.004	33.7	0.23	-0.025	0.0002	-0.062	0.0011	1.568	0.010
4.425	0.006	22.7	0.54	-0.026	0.0007	0.006	0.0009	0.761	0.009
5.845	0.007	14.4	0.52	-0.050	0.0013	-0.083	0.0018	1.128	0.015
6.049	0.001	92.1	0.55	-0.027	0.0002	-0.047	0.0002	0.896	0.002
6.707	0.002	15.4	0.07	0.126	0.0004	-0.052	0.0004	1.040	0.008
7.440	0.008	26.0	0.17	-0.041	0.0004	-0.047	0.0004	1.928	0.031
7.753	0.001	85.1	0.19	-0.090	0.0002	-0.028	0.0002	0.802	0.001
7.791	0.163	27.1*	1006.4	0.122	0.0009	-0.048	0.0009	0.24	2.2
8.135	0.021	8.5*	0.05	-0.012	0.0004	-0.112	0.0007	5.75	0.12
8.908	0.001	37.0	0.07	0.120	0.0002	-0.051	0.0002	0.942	0.003
9.582	0.002	38.1	0.06	-0.094	0.0002	-0.031	0.0002	1.248	0.006
10.637	0.001	98.3	0.67	0.046	0.0002	-0.041	0.0002	0.847	0.002
10.872	0.002	54.9	0.67	0.029	0.0004	-0.009	0.0004	0.990	0.004
10.944	0.001	66.8	0.08	-0.094	0.0002	-0.035	0.0002	0.907	0.002
11.873	0.001	60.4	0.10	0.038	0.0002	-0.030	0.0002	0.828	0.002
12.779	0.001	78.2	0.07	-0.095	0.0002	-0.038	0.0002	0.909	0.001
14.243	0.002	18.0	0.12	-0.007	0.0007	-0.008	0.0007	0.541	0.003
15.295	0.006	34.2	0.06	0.006	0.0002	0.000	0.0002	2.220	0.017
16.215	0.002	23.7	0.12	-0.054	0.0004	-0.082	0.0007	0.835	0.004
16.280	0.003	41.4	0.32	-0.011	0.0004	-0.008	0.0004	0.688	0.004
16.855	0.001	202.3	0.27	0.004	0.0002	0.006	0.0002	0.702	0.0008
16.938	0.001	94.7	0.07	-0.029	0.0002	-0.153	0.0002	1.223	0.001
18.714	0.005	18.3	0.17	-0.014	0.0004	-0.073	0.0004	1.604	0.012
19.074	0.001	90.5	0.18	-0.011	0.0002	-0.106	0.0002	0.709	0.001

**Fig. 4.** Same as Fig. 2, for U Her. Each spot is labelled with the velocity at the Gaussian center, in km s⁻¹.

shell. The strength of the blue peak can be explained by maser amplification of the continuum emission from the central star in the radial direction towards the observer. The relatively strong emission at the stellar velocity shows that tangential amplifica-

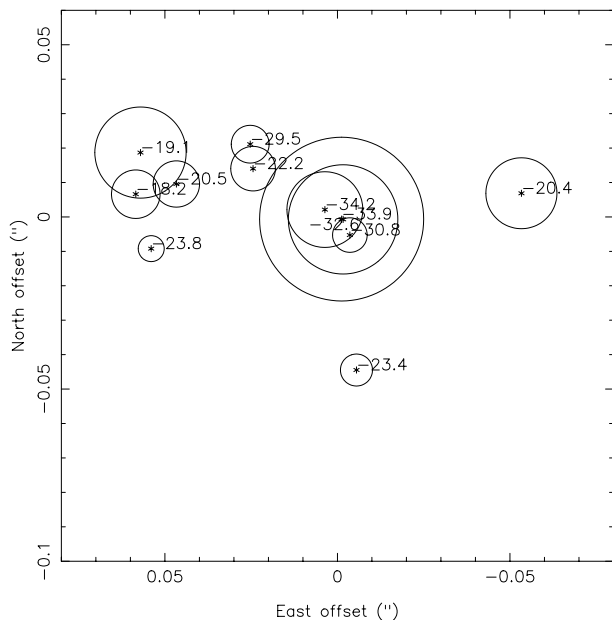
**Fig. 5.** Same as Fig. 3, for U Her.

tion may also play a role. There is no detected emission from the red “cap”, expected at -9.2 km s⁻¹. Engels et al. (1988) did not detect any H₂O maser emission at this velocity either.

Sloutmaker et al. (1985) show that the expansion velocity of the OH maser shell in IRC +60169 is about 12.5 km s⁻¹. The terminal velocity of the envelope, as obtained from CO observations, could be in the range of 15 km s⁻¹ (Margulis et al. 1990) to 19.7 km s⁻¹ (Nyman et al. 1992). Loup et al. (1993) find CO within a radius of $1.6 \cdot 10^{17}$ cm. We find that the H₂O maser distribution may be fitted by a spherical shell centered at the blue “cap” position (the image center), with radius 0.055 and expansion velocity 12.5 km s⁻¹, consistent with the values given by Engels et al. (1988). This shell is sufficiently far away from the star for its expansion to be mostly radial; it would

Table 3. Same as Table 2, for U Her

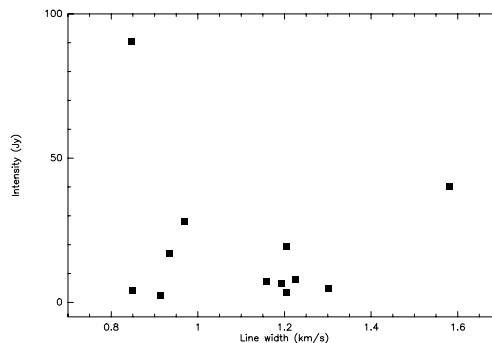
V_{LSR}	$\sigma_{V_{\text{LSR}}}$	I (Jy)	σ_I	$\Delta\alpha$ (")	$\sigma_{\Delta\alpha}$	$\Delta\delta$ (")	$\sigma_{\Delta\delta}$	Δv	$\sigma_{\Delta v}$
-10.186	0.001	1.3	0.01	-0.080	0.0004	0.059	0.0004	0.825	0.003
-14.110	0.001	3.7	0.01	-0.076	0.0002	0.085	0.0002	1.043	0.003
-14.607	0.001	117.2	0.22	0.002	0.0002	-0.001	0.0002	0.586	0.0002
-14.795	0.002	2.0	0.01	0.037	0.0004	0.088	0.0004	1.914	0.008
-15.015	0.003	2.0	0.01	-0.102	0.0006	0.043	0.0006	1.020	0.007
-15.084	0.001	97.7	0.77	0.002	0.0002	-0.001	0.0002	0.729	0.002
-15.130	0.011	1.7*	0.01	-0.048	0.0004	0.087	0.0004	4.089	0.041
-15.317	0.002	76.9	0.67	-0.004	0.0002	0.001	0.0002	0.860	0.001
-15.591	0.003	2.9	0.01	-0.004	0.0002	0.007	0.0002	3.038	0.018
-16.156	0.004	2.0*	0.01	-0.075	0.0002	0.015	0.0004	2.463	0.016
-16.554	0.004	1.3	0.01	-0.063	0.0006	0.090	0.0006	1.041	0.012
-17.689	0.002	2.6	0.01	-0.038	0.0002	0.106	0.0002	1.281	0.007
-18.277	0.001	11.0	0.01	-0.022	0.0002	-0.009	0.0002	0.887	0.0006

**Fig. 6.** Same as Fig. 4, for IRC +60169.

be consistent with a shell smaller than the OH one, that has not reached the terminal velocity. At the assumed distance of 690 pc, the H_2O shell has a radius of $5.7 \cdot 10^{14}$ cm, a small value for a supergiant star. However, the distance quoted has been obtained from the bolometric flux of IRC +60169, assuming a luminosity of $10^4 L_\odot$ (Loup et al. 1993). If we would use instead a luminosity of $10^5 L_\odot$ (a more reasonable value for a supergiant star), we would obtain a H_2O maser shell of radius $\sim 1.8 \cdot 10^{15}$ cm.

4.4. RX Boo

RX Boo is a semiregular variable star. It displays strong, variable H_2O maser emission, but no OH masers have ever been detected. We have been able to model the H_2O maser emission in RX Boo in terms of 15 Gaussian sources, down to the 0.5 Jy level (see Table 5). The resulting map is shown in Fig. 8. Inspection of

**Fig. 7.** Same as Fig. 3, for IRC +60169.

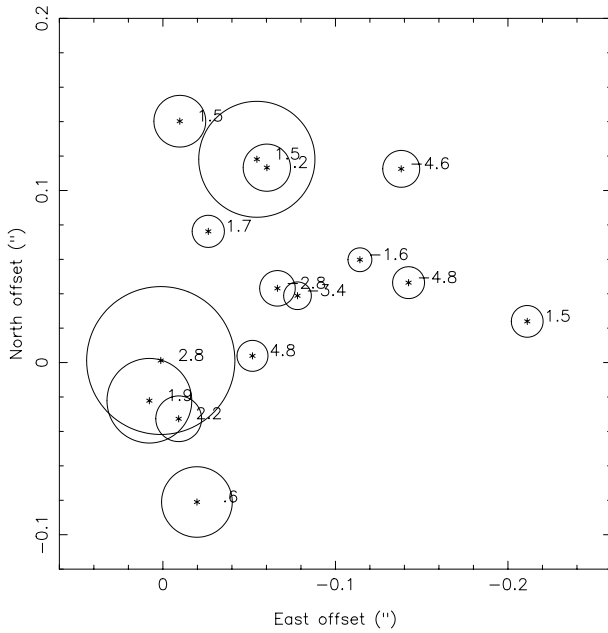
a few pixels demonstrate that these sources are real, and that they can be separated in a position-velocity analysis even if most spots are spatially blended. The extreme velocity features appear close to the H_2O maser distribution centroid, while the features around the systemic velocity are distributed in a ring-like structure. We have been able to fit the data to a spherical shell centered at $(-0''.100, 0''.015)$, with radius $0''.115$ ($2.4 \cdot 10^{14}$ cm at the adopted distance of 141 pc), and an expansion velocity of 4 km s^{-1} . The best fit is obtained if we consider the systemic velocity to be $v_{\text{LSR}} = 1 \text{ km s}^{-1}$. Most of the spots seem to fall near the model of the shell; the small differences could be caused by turbulent motions in the shell. The maser linewidths obtained with “FG3” are displayed in Fig. 9; the fact that the strongest features have narrower linewidths may indicate that these masers are unsaturated (see Sect. 5.2).

Our results are consistent with those of Engels et al. (1993), who fit a shell of $0''.13$ radius and an expansion velocity of $\sim 6 \text{ km s}^{-1}$. This is smaller than the expansion velocity derived from the thermal emission of SiO (9 km s^{-1} , see Lucas et al. 1992, who also report that the emission extends to $1''.4$, or $3 \cdot 10^{15}$ cm), and also smaller than the terminal expansion velocity of the shell $\sim 10 \text{ km s}^{-1}$ as obtained from CO, produced within $5.6 \cdot 10^{16}$ cm (rescaling from Loup et al. 1993, as explained before).

The H_2O spectrum of RX Boo has undergone strong changes in the last 15 years: a strong feature at 6 km s^{-1} mapped by

Table 4. Same as Table 2, for IRC +60169

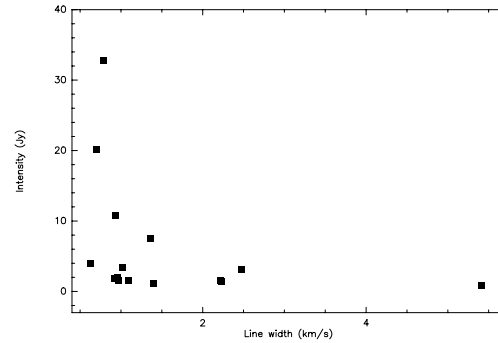
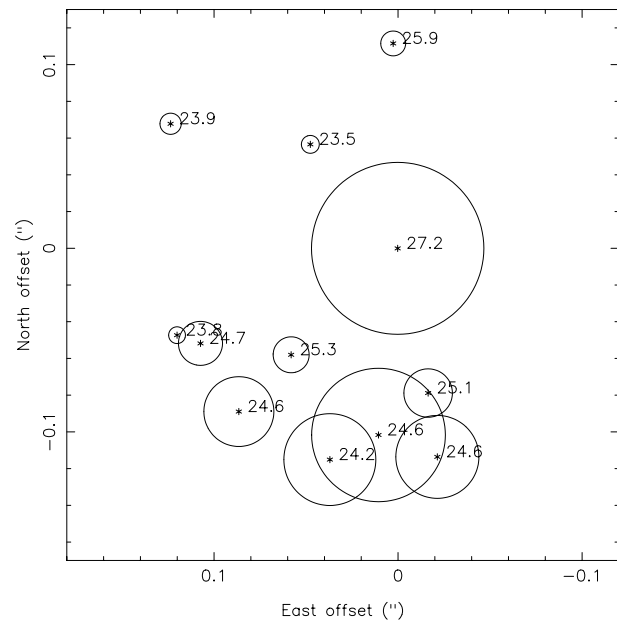
V_{LSR}	$\sigma_{V_{\text{LSR}}}$	I (Jy)	σ_I	$\Delta\alpha''$	$\sigma_{\Delta\alpha}$	$\Delta\delta''$	$\sigma_{\Delta\delta}$	Δv	$\sigma_{\Delta v}$
-18.152	0.079	7.9	0.58	0.058	0.0023	0.007	0.0027	1.23	0.13
-19.062	0.013	28.0	0.97	0.057	0.0007	0.019	0.0011	0.97	0.03
-20.361	0.005	17.0	0.30	-0.053	0.0022	0.007	0.0013	0.93	0.01
-20.457	0.022	7.2	0.30	0.047	0.0047	0.010	0.0027	1.16	0.08
-22.232	0.021	6.7	0.19	0.024	0.0029	0.014	0.0032	1.19	0.07
-23.378	0.055	3.5	0.43	-0.006	0.0099	-0.044	0.0086	1.20	0.13
-23.827	0.056	2.3	0.45	0.054	0.0182	-0.009	0.0135	0.91	0.13
-29.527	0.028	4.8	0.15	0.025	0.0036	0.021	0.0036	1.30	0.09
-30.840	0.029	4.0	0.22	-0.004	0.0056	-0.005	0.0054	0.85	0.08
-32.615	0.017	40.2	0.33	-0.002	0.0004	-0.001	0.0004	1.58	0.05
-33.899	0.004	90.4	7.78	-0.001	0.0009	-0.001	0.0007	0.85	0.02
-34.191	0.143	19.3	6.65	0.004	0.0020	0.002	0.0018	1.20	0.10

**Fig. 8.** Same as Fig. 4, for RX Boo.

Johnston et al. (1985) is not present in our data. Bowers et al. (1993), who studied the H_2O maser emission in this source with the same instrumental configuration, did not detect this feature either, but report a 27 Jy feature around -1.5 km s^{-1} that we don't see. Their map shows that the velocity groups of redshifted and blueshifted maser features are separated $0''.15$. However, they were not able to estimate the position of the central star relative to the maser spots.

4.5. R Cas

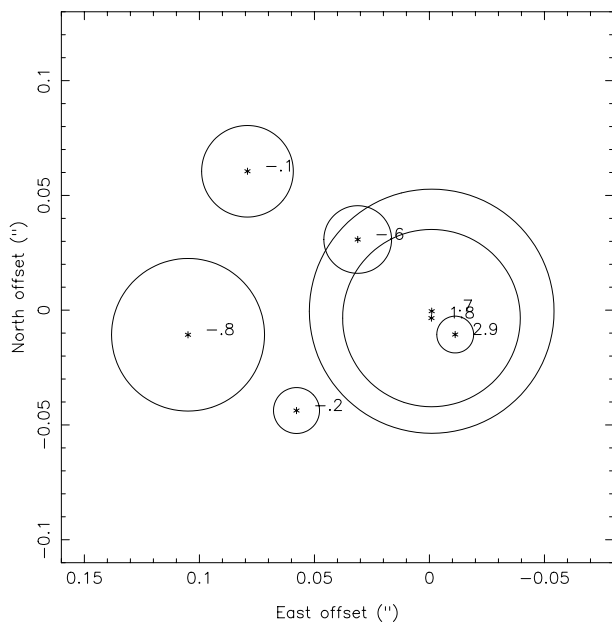
We performed three snapshot observations of duration 6.5 minutes each of the Mira-type star R Cas, and the resulting map is shown in Fig. 10. We have modelled the H_2O maser distribution in R Cas in terms of 12 Gaussian sources with the program “FG3” (see Table 6). Such a distribution is compatible with a shell located near the red peak position (at the image center), with a radius of $0''.13$ ($3.6 \cdot 10^{14} \text{ cm}$ for a distance of 184 pc) and

**Fig. 9.** Same as Fig. 3, for RX Boo.**Fig. 10.** Same as Fig. 4, for R Cas.

an expansion velocity of only 3 km s^{-1} , significantly smaller than the 10 km s^{-1} measured for thermal SiO by Lucas et al. (1992), and the 12 km s^{-1} for CO by Loup et al. (1993). The H_2O maser shell is also contained inside the region of thermal SiO emission (with a radius of $2.5 \cdot 10^{15} \text{ cm}$), and that of CO ($7.6 \cdot 10^{16} \text{ cm}$).

Table 5. Same as Table 2, for RX Boo

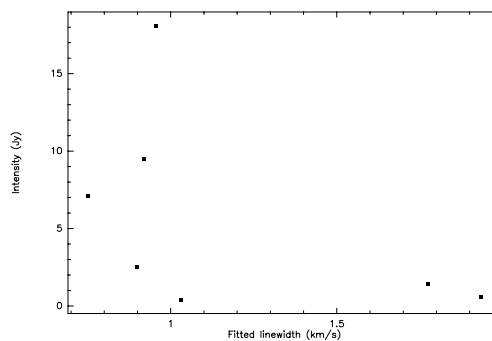
V_{LSR}	$\sigma_{V_{\text{LSR}}}$	I (Jy)	σ_I	$\Delta\alpha('')$	$\sigma_{\Delta\alpha}$	$\Delta\delta('')$	$\sigma_{\Delta\delta}$	Δv	$\sigma_{\Delta v}$
-4.784	0.005	1.5	0.02	-0.142	0.0006	0.046	0.0011	1.096	0.014
-4.627	0.003	2.0	0.02	-0.138	0.0005	0.113	0.0008	0.959	0.007
-3.410	0.077	1.1	0.10	-0.078	0.0011	0.039	0.0008	1.40	0.11
-2.764	0.008	1.9	0.17	-0.066	0.0016	0.043	0.0008	0.92	0.03
-1.590	0.031	0.9*	0.01	-0.114	0.0005	0.060	0.0005	5.41	0.14
0.155	0.002	3.3	0.01	-0.060	0.0003	0.113	0.0003	1.020	0.005
0.572	0.001	7.5	0.02	-0.020	0.0002	-0.081	0.0002	1.363	0.003
1.473	0.001	20.2	0.08	-0.054	0.0002	0.118	0.0002	0.704	0.0009
1.481	0.003	1.5	0.01	-0.211	0.0005	0.024	0.0005	0.970	0.008
1.488	0.001	4.0	0.08	-0.010	0.0008	0.140	0.0005	0.633	0.004
1.725	0.010	1.5	0.01	-0.026	0.0006	0.076	0.0006	2.22	0.03
1.854	0.001	10.7	0.05	0.008	0.0002	-0.022	0.0002	0.938	0.003
2.159	0.009	3.1	0.06	-0.009	0.0003	-0.033	0.0005	2.48	0.04
2.753	0.001	32.8	0.03	0.001	0.0002	0.001	0.0002	0.789	0.0007
4.755	0.007	1.4	0.01	-0.052	0.0003	0.004	0.0003	2.24	0.03

**Fig. 11.** Same as Fig. 4, for R LMi.

The maser linewidths obtained with “FG3” indicate that these masers are possibly unsaturated, with exponential amplification causing the narrower linewidths of the strongest features (see Sect. 5.2).

4.6. R LMi

The 3D Gaussian fitting program “FG3” successfully found, down to the 0.4 Jy level, seven Gaussians as responsible for the maser emission in the Mira-type star R LMi. Despite that the inspection of the results (see Fig. 11) suggests the existence of a ring-like structure, we have not been able to fit a shell to the spot distribution, and we do not have any easy clue about the spatial structure of the maser environment. Bujarrabal & Alcolea (1991) studied the CO emission but could only state that

**Fig. 12.** Same as Fig. 3, for R LMi.

its extent should be smaller than $8''$. The SiO maser emission at 43 GHz in R LMi was undetected in a VLBI experiment with maximum fringe spacing of 4.2 mas (Colomer et al. 1992). In case the non detection of VLBI fringes were due to the fact that the source had been resolved out, this would set a lower limit to the size of the masing region of $\sim 2 \cdot 10^{13}$ cm at the assumed distance of 355 pc.

4.7. Other sources

Table 9 summarizes the observational status of the other sources. No H_2O maser emission was found towards EU And (a carbon-type star), while the emission was very compact towards the other sources and the VLA A-configuration did not provide enough spatial resolution to distinguish any structure. The obtained beam sizes, which are upper limits for the sizes of the H_2O maser regions, are quoted.

5. Discussion

5.1. Morphology of the maser regions

The spatial and velocity distribution of H_2O maser spots has been determined in 5 stars using the “FG3” program, described in the appendix. In most of the cases, we have been able to

Table 6. Same as Table 2, for R Cas

V_{LSR}	$\sigma_{V_{\text{LSR}}}$	I (Jy)	σ_I	$\Delta\alpha('')$	$\sigma_{\Delta\alpha}$	$\Delta\delta('')$	$\sigma_{\Delta\delta}$	Δv	$\sigma_{\Delta v}$
23.496	0.009	0.4*	0.01	0.048	0.0006	0.057	0.0006	2.46	0.04
23.765	0.024	0.4	0.01	0.120	0.0007	-0.047	0.0007	1.96	0.07
23.896	0.007	0.6*	0.01	0.124	0.0004	0.068	0.0004	2.62	0.03
24.223	0.001	11.1	0.02	0.037	0.0002	-0.115	0.0002	0.720	0.0009
24.590	0.001	6.4	0.02	0.087	0.0002	-0.089	0.0002	0.858	0.0015
24.627	0.001	9.1	0.05	-0.021	0.0002	-0.114	0.0002	0.678	0.0008
24.650	0.001	23.4	0.05	0.011	0.0002	-0.102	0.0002	0.712	0.0005
24.692	0.001	2.5	0.02	0.107	0.0004	-0.052	0.0004	0.735	0.003
25.052	0.002	3.1	0.02	-0.016	0.0002	-0.079	0.0002	0.822	0.003
25.304	0.003	1.7	0.01	0.058	0.0002	-0.058	0.0002	1.312	0.008
25.933	0.003	0.8	0.01	0.003	0.0004	0.112	0.0004	1.315	0.011
27.201	0.001	39.0	0.01	0.000	0.0002	0.000	0.0002	0.659	0.0001

Table 7. Same as Table 2, for RLMi

V_{LSR}	$\sigma_{V_{\text{LSR}}}$	I (Jy)	σ_I	$\Delta\alpha('')$	$\sigma_{\Delta\alpha}$	$\Delta\delta('')$	$\sigma_{\Delta\delta}$	Δv	$\sigma_{\Delta v}$
2.902	0.014	0.4	0.01	-0.011	0.0010	-0.001	0.0010	1.032	0.033
1.759	0.001	9.5	0.01	-0.001	0.0002	0.007	0.0002	0.919	0.002
0.683	0.001	18.1	0.01	-0.001	0.0002	0.010	0.0002	0.956	0.0008
-0.072	0.001	2.5	0.01	0.079	0.0002	0.071	0.0002	0.900	0.003
-0.150	0.008	0.6	0.01	0.058	0.0006	-0.034	0.0006	1.935	0.022
-0.629	0.005	1.4	0.01	0.031	0.0004	0.041	0.0004	1.775	0.016
-0.807	0.001	7.1	0.01	0.105	0.0002	-0.001	0.0002	0.750	0.0008

locate the H₂O masers on an expanding shell around the central star (see Table 8). The semiregular stars R Crt and RX Boo, the supergiant IRC +60169, and the Mira R Cas, are in agreement with this kinematical scenario. However, for U Her we have not been able to fit this simple model. In all cases, the H₂O maser emission is not produced in a continuous shell but is rather clumpy. The VLA lacks the resolution needed to resolve individual compact maser spots.

Water masers in AGB stars appear distributed in a region of 4–7 10¹⁴ cm (30 to 48 AU) in extent. This result is consistent with previous measurements (see Sect. 1).

Fig. 13 demonstrates that the size of the H₂O maser region increases with the mass-loss rate. This effect was predicted by Cooke & Elitzur (1985), and has been observed as well in other sources by Lane et al. (1987) and Yates & Cohen (1994). A least-squares fit to the points,

$$\log R(\text{AU}) = (0.456 \pm 0.008) \log \dot{M} (M_{\odot}/\text{yr}) + (4.07 \pm 0.05) \quad (2)$$

is represented by a solid line in Fig. 13. If we assume that the H₂O maser needs a certain density to turn on, as predicted by the models, this relation means that such a density is attained at a distance $r \propto \dot{M}^{0.5}$, which is the value expected for the expansion at constant velocity (such as that often found in circumstellar shells). See Sect. 5.3 for more details.

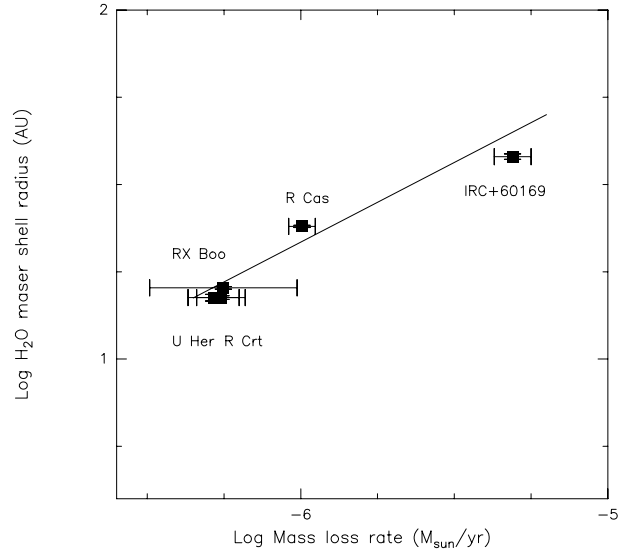


Fig. 13. Fitted radii of the H₂O masers shell, plotted against the stars' mass-loss rates (rescaled from Loup et al. 1993; see Sect. 4).

5.2. Maser linewidths and saturation

We have been able to accurately determine the linewidths of the individual H₂O maser features. In three sources there is a clear anticorrelation between intensity and width of the features (see Figs. 5, 9, and 14 for U Her, RX Boo, and R Cas, respectively).

Radiative transfer theory can explain this effect. It is well known that the profile of a maser transition is approximately

Table 8. Model parameters inferred in the analysis of the H₂O maser sources with program “FG3”

Source	# spots	DR ^a	Shell	Center position ^b	R_s ^c	R_s ^d	R_s ^e	v_{LSR}	v_{exp}
IRC +60169	12	2525	thin	(0, 0)	55	5.7	38	-20	12.5
R Crt	26	3353	thin	(-23, -65)	82	2.3	15	10.8	8
RX Boo	15	741	thin	(-100, 15)	115	2.4	16	1	4
U Her	13	3483	thick	(-50, 50)	45–70	2.3–3.6	15–24	-15	6
R Cas	12	920	thin	(0, 0)	130	3.6	24	24	3

^a Dynamic range in the map.

^b Shell center position (α , δ) in milliarcseconds relative to the spot chosen as reference.

^c Radius of the fitted shell, R_s , in milliarcseconds.

^d R_s , in units of 10^{14} cm.

^e R_s , in AU.

Table 9. Other sources

Source	α (2000.0)	δ (2000.0)	Comments	Beam (mas)
U Ori	05 55 49.20	+20 10 30.00	Unresolved	150 × 90 (48 deg)
OH231.8 + 4.2	07 42 16.84	-14 42 50.99	Unresolved	219 × 95 (38 deg)
R LMi	09 45 34.10	+34 30 44.00	no shell fitting	
R Aql	19 06 22.00	+08 13 48.00	Unresolved	129 × 79 (56 deg)
V778 Cyg	20 36 07.42	+60 05 26.26	Unresolved	105 × 76 (36 deg)
EU And	23 20 01.93	+47 14 25.81	Undetected	—

Gaussian and, for unsaturated amplification, has a linewidth (FWHM) given by

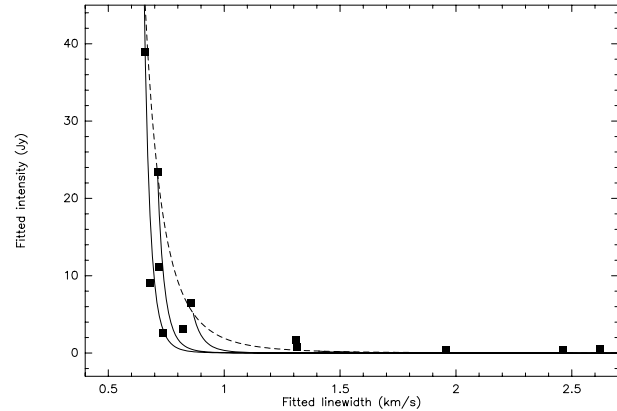
$$\Delta\nu \approx \frac{\Delta\nu_D}{\sqrt{|\tau_{\nu_0}|}} \quad (3)$$

(Goldreich & Kwan 1974) where $\tau_\nu = k_\nu x$, being k_ν the opacity of the medium and x the amplification path length. The linewidth decreases as the maser grows until the center of the maser line begins to saturate (i.e. reaches its maximum efficiency). The linewidth can then broaden since the wings of the line continue to experience exponential growth and the center of the line grows more slowly, until the linewidth again equals the thermal (Doppler) width $\Delta\nu_D$. Therefore, it is expected that unsaturated masers should display a strong correlation between the strongest features and those with the narrowest linewidths, while saturated masers might always display linewidths approaching the thermal width.

The anticorrelation between the intensity and width of the maser features is seen qualitatively in several cases discussed in Sect. 4. We may now check quantitatively the consistency of the measured intensities and linewidths. We will calculate the opacities needed to explain both the expected linewidths (according to Eq. 3) and the brightness temperatures that corresponds to the 22 GHz H₂O maser flux densities:

$$T_B(\text{K}) = 8.94 \cdot 10^8 \frac{1}{\theta(\text{mas})^2} I(\text{Jy}) \sim T_x e^{-\tau}. \quad (4)$$

The individual maser spots appear unresolved in our data (due to the limited spatial resolution of the VLA, ~ 70 mas). Some authors have reported spot sizes as small as ~ 1 mas (Imai et al. 1997); however they detect only about 10% of the total flux observed with single-dish or the VLA. We thus assume that those

**Fig. 14.** Same as Fig. 3, for R Cas. The dotted line represents the locus of maximum expected maser intensity (see Sect. 5.2).

VLBI observations are sensitive to the smallest structures, while some other more extended (and intense) features are resolved out. The spot diameter must be then significantly larger than 1 mas: an upper limit to the spot sizes might be ~ 30 mas (or we would start seeing resolution effects in the data, as our minimum fringe spacing is 70 mas). We will also assume an excitation temperature $T_x \sim -100$ K in the H₂O maser region. (Note that the opacity values obtained are not very sensitive to the exact value of the temperature adopted.)

For each maser feature, the opacity needed to explain its intensity allows us to determine, from the observed linewidth $\Delta\nu$ and using Eq. 3, the original linewidth of the H₂O transition before the effects of line narrowing, $\Delta\nu_D$, the local velocity dispersion. The obtained values, of the order of 2–4 km s⁻¹, are too large to be thermal widths given the conditions in these

regions ($T \leq 700$ K, thus $\Delta v_D \leq 1.3$ km s $^{-1}$), and can best be explained by turbulent motions. Note that these values are comparable to the largest linewidths measured in our data.

Of course, for each value of the local velocity dispersion we can get a variety of values of $\Delta\nu$ and T_B , depending on the opacity, which itself depends on the various sizes and physical conditions in the emitting clumps. In any case, we expect that $\tau = C/\Delta v_D$ for each component, where the constant C includes the pumping efficiency of the maser and the column density. Both parameters cannot grow indefinitely, so we can assume that there is a maximum value of C that is independent of the “original” Δv_D . This maximum C would define a line in the T_B versus Δv diagram over which we do not expect to find observational points.

Fig. 14 displays the locus of maximum intensities for each linewidth of any maser feature, calculated using one intense spot as a calibrator of the constant C defined above. As we see, practically all features lie under the dashed line, particularly the most reliably determined ones. The consistency of our expectations on the relation between T_B and $\Delta\nu$ and the empirical results strongly suggest that our assumptions on the line formation mechanisms are correct, and, in particular, that the H₂O masers are unsaturated (see also the discussion in Reid & Menten 1990).

Another point of interest is the fact that, despite the large values of the opacity found using Eq. 4, there are no features with spectral width smaller than 0.5 km s $^{-1}$. One possible explanation would be the existence of hyperfine structure in the $J = 6_{16} \rightarrow 5_{23}$ line of H₂O (see Fig. 1 in Walker, 1984): the line breaks into six hyperfine components, and the velocity separation among the three strongest ones are 0.445, 0.580, and 1.025 km s $^{-1}$ (Sullivan 1973). Thus the activation of any two of these lines would prevent the existence of maser features of linewidth narrower than ~ 0.5 km s $^{-1}$.

The hyperfine structure could also be the reason for the existence of weak features with moderate linewidths (but larger than the Doppler value). The misidentification and further modeling of two (or three) of these lines as a single feature would cause an increase by a factor of ~ 2 in its wrongly fitted linewidth.

5.3. The location of the H₂O masers in circumstellar envelopes around red giant stars

As we have seen, we find that in four AGB stars (i.e. excluding the red supergiant IRC +60169) the H₂O masers occupy a region with diameter between 4 and 7 10^{14} cm. These values are in agreement with previous estimates, that yield diameters for the H₂O emitting regions in these objects ranging between 10^{14} cm and 10^{15} cm (see Sect. 1). We note that such values only apply for optically identified red giants, since no VLBI observations of H₂O masers in very reddened OH/IR stars have been published. On the other hand, in red supergiants the extent of the H₂O maser region is significantly larger (Sects. 1 and 4.3).

It is interesting to compare the extent of the H₂O maser emission with the values found for the diameter of the inner part of the envelope, in which the dust grains are not completely

formed and the gas has not yet reached its terminal (high) velocity. (Such a comparison can only be done statistically, since only for a few objects both parameters have been measured.) Studies of SiO masers in Mira-type stars have shown that the emission is distributed in a ring, with diameters ~ 10 AU ($1.5 \cdot 10^{14}$ cm; see Diamond et al. 1994; Colomer et al. 1996), which reaches ~ 60 AU for the supergiant VX Sgr (Greenhill et al. 1995). On the other hand, Danchi et al. (1994) have found from mid-infrared ($10\mu\text{m}$) interferometry that the inner dust diameter in O-rich AGB stars ranges between 1 and 6 10^{14} cm. A similar result was found by Dyck et al. (1984). The measurement of the extent of the SiO emission is an independent (though less direct) way to estimate this parameter, since, in O-rich AGB envelopes, the SiO emission is expected to come only from circumstellar regions in which the dust is not yet formed. Lucas et al. (1992) have found that most of the SiO emission comes from regions about 10^{15} cm wide. These authors also found, from the behavior of the different velocity components, that in such a region there is still a significant velocity gradient, i.e. that the expansion velocity has not yet reached its final value.

Therefore, the high spatial resolution images indicate that the H₂O maser emission comes from inner regions of the circumstellar shells, quite comparable in extent with the grain formation regions.

This result is confirmed by the behavior of the H₂O line profiles in not very reddened AGB stars (see Engels & Lewis 1996, and Sect. 4), which in general show a very small extent in velocity spread and no clear two-peak structure. This property is in fact characteristic of objects with low mass-loss rates, since Engels & Lewis find that the H₂O profiles tend to show the characteristic two-peak structure for the denser envelopes of OH/IR stars. Moreover, the separation of the peaks is found to increase with the mass-loss rate, approaching that of the OH maser lines. The narrow and peculiar H₂O profiles in optically identified red giants can be easily understood if the maser arises from the inner dust formation regions. In these regions the expansion velocity is significantly smaller, and we expect the presence of a strong radial acceleration, which implies tangential maser amplification (for values of the logarithmic velocity gradient, $r/v dv/dr$, larger than 1; where v is the expansion velocity and r is the distance to the center). Also, in these inner regions shock waves may be propagating, yielding nonmonotonic velocity fields and complex line profiles.

The location of the H₂O masers inside the dust formation radius, for objects with relatively low mass-loss rates, is also compatible with the results of pumping model calculations. Cooke & Elitzur (1985) found that for mass-loss rates smaller than 10^{-6} M $_{\odot}$ /yr the density needed to pump the H₂O masers is only attained at distances $< 10^{15}$ cm. The density is the critical parameter for the H₂O maser pumping, as it is essentially collisional. If the mass-loss rate in an object is constant with time, the density varies as $\rho \propto \dot{M}/r^2v$, therefore the point at which a certain density is attained depends on the velocity field, which is not well known in the inner regions. But we can assume, as these authors did and we have discussed above, that for distances larger than 10^{15} cm the velocity is practically constant.

Therefore, the theoretical limit on the extent given by the model calculations holds in our case, independently of the field in the inner regions. In these regions the expansion velocity must increase outwards, from about zero to the final velocity. So, the critical density to pump the maser is actually attained at some point in this regions (even if not at the same distance as that deduced by Cooke & Elitzur), where the pump properties would be similar to those calculated by those authors.

5.4. Other applications of the 3D spectral line emission fitting code

We have applied our computer code to study the structure of several H₂O maser emitting sources, and discussed the implications in the preceding sections. The “FG3” program allows to disentangle the different components (spots) that form a maser region. This is also of great importance in the understanding of the maser structure because it provides information to distinguish whether these masing regions are due to condensations, or they are the result of velocity coherence along the field of view. In the first case, we would expect a large masing area with different velocity components, while in the second case the maser spots would appear much more compact, and the velocity coverage would be much smaller.

On the other hand, the method may be applied to the study of sources that show differences when observed with different spatial resolutions; the program would provide, in all cases, the basic source information that may be used to recreate an image at any desired resolution. Moreover, it could be used for comparing the results obtained with moderate resolution instruments, such as the VLA, which is sensitive to extended emission, to those obtained by high resolution techniques such as VLBI, sensitive only to the most compact structures.

6. Conclusions

We have performed observations of the H₂O maser emission in the circumstellar envelopes of 11 late-type stars with the VLA. In order to study the maser spatial and velocity morphology, we have constructed a computer program (“FG3”, described in the appendix). Using this program, we have been able to place the H₂O masers on an expanding shell around the central star in five cases (IRC +60169, R CrT, RX Boo, U Her, and R Cas, see Table 8), despite of the fact that the emission is rather clumpy and the shells appear incomplete. A characteristic radius of ~ 20 AU emerges for H₂O maser emission in AGB stars. At this distance from the star, dust is still forming (or dust grains are still getting larger), so H₂O masers are in the region of acceleration, where the expanding envelope has not reached its terminal velocity. Moreover, our maps confirm that there is a correlation between the overall sizes of the H₂O maser regions and the mass-loss rate from the star, in agreement with the theoretical predictions. Note that the VLA lacks the resolution needed to resolve the individual compact maser spots.

An important advantage in the use of “FG3”, over earlier studies, is the much better spectral linewidth estimate, com-

pared to the usual procedure of fitting positions in each spectral channel map and later using these results to infer linewidths. The maser linewidth contains information about the physical conditions in the region where the maser phenomena occur. In particular, it provides a powerful tool to discriminate whether or not these masers are saturated. For completely unsaturated masers, maser theory predicts that the strongest features must have also the narrowest linewidths. We clearly see evidence for line narrowing toward U Her, RX Boo, and R Cas, which indicates that these masers are unsaturated.

Appendix A: the 3D Gaussian fitting program “FG3”

We have developed a computer program for the inspection and analysis of spectral line cubes. In general, a spectral line cube is a 3-dimensional (3D) array in which two of the dimensions are sky spatial coordinates (usually the right ascension α and the declination δ or functions of them) and the third dimension is velocity or frequency. The cube stores the intensity distribution of the source.

In the study of astronomical maser emission, we can model the intensity distribution as produced by a number of (3D Gaussian) spots. A spatially unresolved 3D Gaussian feature can be specified by eight parameters, which are the Gaussian peak intensity ($I_o = I(\alpha_o, \delta_o, v_o)$), the Gaussian position center ((α_o, δ_o)) and velocity (v_o), the full linewidth at half power (σ_v) and, finally, the Gaussian spatial form, which is determined by the interferometer beam shape (more specifically by the restoring beam); in a general case, it is a tilted ellipse specified by three parameters (the semimajor axis b_{maj} , the semiminor axis b_{min} , and the tilting angle θ , defined, for example, counterclockwise from the X-axis to the major axis). A maser feature can be described, then, as

$$I(\alpha, \delta, v) = I_o \exp \left\{ -\ln 2 \left(A(\alpha - \alpha_o)^2 + B(\delta - \delta_o)^2 + C(\alpha - \alpha_o)(\delta - \delta_o) + 4 \left(\frac{v - v_o}{\sigma_v} \right)^2 \right) \right\} \quad (\text{A.1})$$

where

$$A = \frac{b_{min}^2 \cos^2(\theta) + b_{maj}^2 \sin^2(\theta)}{b_{maj}^2 b_{min}^2} \quad (\text{A.2})$$

$$B = \frac{b_{min}^2 \sin^2(\theta) + b_{maj}^2 \cos^2(\theta)}{b_{maj}^2 b_{min}^2} \quad (\text{A.3})$$

$$C = \frac{2(b_{min}^2 - b_{maj}^2) \cos(\theta) \sin(\theta)}{b_{maj}^2 b_{min}^2}. \quad (\text{A.4})$$

The derivatives of this 3D Gaussian function with respect to the eight parameters are

$$\frac{dI(\alpha, \delta, v)}{dI_o} = I(\alpha, \delta, v)/I_o$$

$$\frac{dI(\alpha, \delta, v)}{d\alpha_o} = \ln 2 I(\alpha, \delta, v) (2A(\alpha - \alpha_o) + C(\delta - \delta_o))$$

$$\frac{dI(\alpha, \delta, v)}{d\delta_o} = \ln 2 I(\alpha, \delta, v) (2B(\delta - \delta_o) + C(\alpha - \alpha_o))$$

$$\frac{dI(\alpha, \delta, v)}{dv_o} = 8 \ln 2 I(\alpha, \delta, v) \left(\frac{v - v_o}{\sigma_v^2} \right)$$

$$\frac{dI(\alpha, \delta, v)}{db_{maj}} = I(\alpha, \delta, v) \frac{2 \ln 2}{b_{maj}^3} \{((\alpha - \alpha_o) \cos(\theta) - (\delta - \delta_o) \sin(\theta))\}^2$$

$$\frac{dI(\alpha, \delta, v)}{db_{min}} = I(\alpha, \delta, v) \frac{2 \ln 2}{b_{min}^3} \{((\alpha - \alpha_o) \sin(\theta) - (\delta - \delta_o) \cos(\theta))\}^2$$

$$\frac{dI(\alpha, \delta, v)}{d\theta} = 2 \ln 2 I(\alpha, \delta, v) \left(\frac{1}{b_{maj}^2} - \frac{1}{b_{min}^2} \right) \{((\alpha - \alpha_o)^2 - (\delta - \delta_o)^2) \cos(\theta) \sin(\theta) + (\alpha - \alpha_o)(\delta - \delta_o)(\sin^2(\theta) - \cos^2(\theta))\}$$

$$\frac{dI(\alpha, \delta, v)}{d\sigma_v} = 8 \ln 2 I(\alpha, \delta, v) \frac{(v - v_o)^2}{\sigma_v^3}$$

A.1. The Levenberg-Marquardt method

The modeling of the spectral line data cube in terms of 3D Gaussian features can be studied as a least-squares fitting problem, noting that the model does not depend linearly with the parameters. The intensity distribution is, in general, a non-linear function of $M = 8G$ parameters (for G Gaussian components),

$$I(\alpha, \delta, v) = I(\alpha, \delta, v; I_{o,i}, \alpha_i, \sigma_{\alpha,i}, \delta_i, \sigma_{\delta,i}, v_i, \sigma_{v,i}, \theta_i; i = 1, \dots, G). \quad (\text{A.5})$$

We are looking for a method to find these parameters (that we will represent as $\mathbf{a} \equiv \{a_i, i = 1, \dots, M\}$ in what follows), error estimates on them, and a statistical measure of the goodness of the fit. Following the discussion and procedures shown in Press et al. (1986), we will identify the probability of the data given the parameters (a mathematically computable number) with the likelihood of the parameters given the data. A maximum likelihood estimate of the model parameters is obtained by minimizing the value of chi-square,

$$\chi^2 = \sum_{j=1}^N \left(\frac{I_j(\alpha_j, \delta_j, v_j) - I(\alpha_j, \delta_j, v_j; \mathbf{a})}{\sigma_j} \right)^2. \quad (\text{A.6})$$

At the chi-square minimum, the following set of nonlinear equations must hold

$$0 = \sum_{j=1}^N \left(\frac{I_j(\alpha_j, \delta_j, v_j) - I(\alpha_j, \delta_j, v_j; \mathbf{a})}{\sigma_j^2} \right) \left(\frac{\partial I(\alpha_j, \delta_j, v_j; \mathbf{a})}{\partial a_k} \right)$$

for $k = 1, \dots, M$. Sufficiently close to the minimum, the nonlinear expression for χ^2 can be well approximated by a quadratic form

$$\chi^2(\mathbf{a}) \approx \gamma - \mathbf{d} \cdot \mathbf{a} + \frac{1}{2} \mathbf{a} \cdot \mathbf{D} \cdot \mathbf{a} \quad (\text{A.7})$$

where \mathbf{d} is a M -vector, \mathbf{D} is a $M \times M$ matrix, and \mathbf{a} is a vector representing the parameters. Because of the nonlinear dependences, the minimization must proceed iteratively. Given the current trial parameters \mathbf{a}_{cur} , an improved trial solution is obtained as

$$\mathbf{a}_{next} = \mathbf{a}_{cur} - \text{constant} \times \nabla \chi^2(\mathbf{a}_{cur}) \quad (\text{A.8})$$

and the procedure is repeated until χ^2 stops decreasing. If the quadratic approximation is a good one, the minimizing parameters can be written directly as

$$\mathbf{a}_{min} = \mathbf{a}_{cur} + \mathbf{D}^{-1} \cdot [-\nabla \chi^2(\mathbf{a}_{cur})] \quad (\text{A.9})$$

where \mathbf{D} is the second derivative matrix (Hessian matrix).

Because we know exactly the analytical form of χ^2 (as it is based on a model function specified by us), we can calculate the gradient

$$\frac{\partial \chi^2}{\partial a_k} = -2 \sum_{i=1}^N \frac{[I_i - I(\mathbf{a})]}{\sigma_i^2} \frac{\partial I(\mathbf{a})}{\partial a_k} \equiv -2 \beta_k \quad k = 1, \dots, M$$

and the Hessian matrix

$$\begin{aligned} \frac{\partial^2 \chi^2}{\partial a_k \partial a_l} &= 2 \sum_{i=1}^N \frac{1}{\sigma_i^2} \left[\frac{\partial I(\mathbf{a})}{\partial a_k} \frac{\partial I(\mathbf{a})}{\partial a_l} - [I_i - I(\mathbf{a})] \frac{\partial^2 I(\mathbf{a})}{\partial a_k \partial a_l} \right] \\ &\equiv 2 \alpha_{kl}. \end{aligned} \quad (\text{A.10})$$

Defining the curvature matrix $[\alpha] = \frac{1}{2} \mathbf{D}$, we can write Eq. A.9 as

$$\sum_{l=1}^M \alpha_{kl} \delta a_l = \beta_k \quad (\text{A.11})$$

where this set is solved for the increments δa_l that, added to the current approximation \mathbf{a}_{cur} , give \mathbf{a}_{next} . On the other hand, Eq. A.8 translates to

$$\delta a_l = \text{constant} \times \beta_l$$

Furthermore, the second derivatives of $I(\mathbf{a})$ can be neglected in the expression for α_{kl} .

The Levenberg-Marquardt method has become the standard of the nonlinear least-squares routines. It varies smoothly between the steepest descent method, used far from the minimum, and the inverse-Hessian method, used as the minimum is approached. By using $\lambda \alpha_{ll} \delta a_l = \beta_l$ and defining a new matrix

$$\begin{cases} \alpha'_{jj} = \alpha_{jj}(1 + \lambda) \\ \alpha'_{jk} = \alpha_{jk} \quad (j \neq k) \end{cases} \quad (\text{A.12})$$

we can rewrite

$$\sum_{l=1}^M \alpha'_{kl} \delta a_l = \beta_k \quad (\text{A.13})$$

so when λ gets very large, the matrix α' becomes diagonally dominant, however when λ approaches zero, we recover Eq. (A.11).

The Levenberg-Marquardt method for obtaining the set of parameters \mathbf{a} that minimize χ^2 and produce the best fit of the model to our data is:

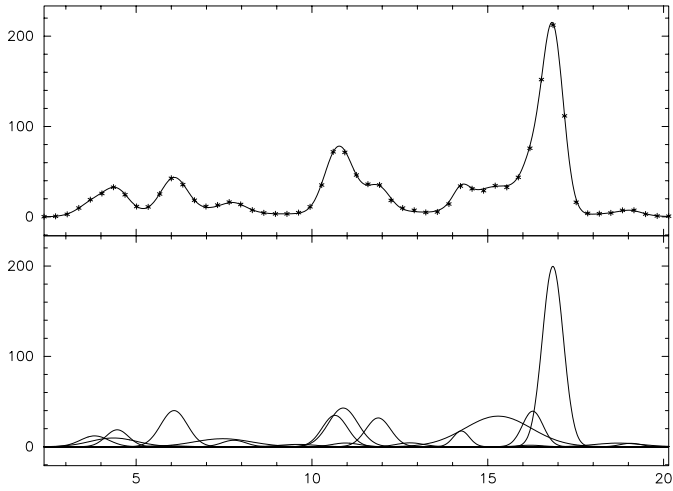


Fig. A.1. Spectrum (intensity in Jy as a function of velocity in km s^{-1}) of the H_2O masers towards R CrA. (Bottom) Individual Gaussians as obtained by “FG3”. (Top) Sum of all Gaussian features, reproducing the observed spectrum.

- Select a set \mathbf{a} of initial trial parameters.
- Calculate $\chi^2(\mathbf{a})$.
- Set a modest value for λ , say $\lambda = 0.001$.
- (†) Solve the linear equations for $\delta\mathbf{a}$ and evaluate $\chi^2(\mathbf{a} + \delta\mathbf{a})$.
- If $\chi^2(\mathbf{a} + \delta\mathbf{a}) \geq \chi^2(\mathbf{a})$ then increase λ and return to (†). Otherwise, decrease λ , update the trial solution $\mathbf{a} \leftarrow \mathbf{a} + \delta\mathbf{a}$, and go back to (†).

The iteration process can stop the second time χ^2 decreases by a negligible amount. Once the acceptable minimum has been found,

$$[C] = [\alpha]^{-1}$$

is the estimated covariance matrix of the standard errors in the fitted parameters \mathbf{a} , calculated by setting $\lambda = 0$.

A.2. Implementation

We have written a computer program to implement the Levenberg-Marquardt method of fitting for the parameters $\mathbf{a} \equiv \{a_i, i = 1, \dots, M\}$ that minimize χ^2 , providing the best fit of the resulting model to our data (see Colomer 1996). The program is fed with the spectral line data stored in FITS format, and performs the fitting to a user-defined function (in our case 3D Gaussians), plus a variety of functions such as guessing of initial parameters, RMS calculation, plotting of data and fitted solutions, model subtraction and inspection of residuals, etc.

The power of “FG3” is shown in Figs. A.1 and A.2.

A.3. Using constraints on the parameters

The process of modeling the intensity distribution of a spectral line source as a function of G tridimensional Gaussian sources requires, in our general case, to find $P = 8G$ parameters. Sometimes, however, we have additional information that constrains the values those parameters can take. One obvious example is

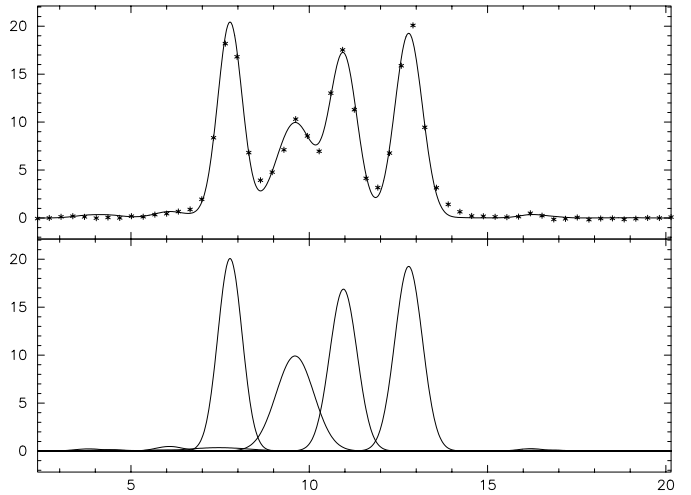


Fig. A.2. Same as Fig. A.1, at position $(-0'16, -0'01)$.

the spatial beam axis b_{maj} and b_{min} , and the tilting angle θ , that we can keep fixed to those of the restoring beam used to obtain the CLEANed data cube for spatially unresolved maser spots.

In other cases, the iterative process may diverge due to an “unfortunate” step in the parameter searching process. We might want to force any parameter value to remain within a given range (what we will call the selected accuracy of that parameter, σ_{a_j}). The way to implement this effect is to calculate χ^2 in two parts, one involving how well the model fits the data (as before), and another involving how close the current parameter values are to the initial ones. One has to be careful, however, as both contributions are not of the same order of magnitude (there are N data points, but only P parameters), and can only be added if they are normalized before in some way. If we want that every σ_{a_j} parameter a_j changes in an iteration counts the same as every σ_j the intensity $I_j(\alpha_j, \delta_j, v_j; \mathbf{a})$ changes, we need to multiply the selected accuracy contribution by the number of data points N , so that

$$\chi^2 = \sum_{j=1}^N \left(\frac{I_j(\alpha_j, \delta_j, v_j) - I(\alpha_j, \delta_j, v_j; \mathbf{a})}{\sigma_j} \right)^2 + N \sum_{j=1}^P \left(\frac{\mathbf{a}_{cur,j} - \mathbf{a}_{ini,j}}{\sigma_{a_j}} \right)^2$$

In order not to use the selected accuracy feature, it will be enough to assign a large value to σ_{a_j} , and that term will not contribute to χ^2 .

A.4. Notes on the reliability of the solutions

The Levenberg-Marquardt method solves a nonlinear problem by an approximation that has some limitations. First, the fitting procedure converges only if the initial values for the parameters are sufficiently close to the real ones. This limitation is overcome in the code by the parameter guessing routines. The number of Gaussian features to fit is a user input parameter, and inspection of the fit residuals is needed to select which value

of such number is best. On the other hand, artifacts may appear when the user specifies a very unappropriate number of Gaussians to fit: a number too large produces very narrow features without any physical meaning, while a number too low results in features of large linewidths. Such features can also be seen in regions of low intensity, as a consequence of the large residuals obtained.

The mathematical solutions should thus be inspected to check that these solutions correspond to real features. One test would be that the fitted Gaussian is associated with a spatial or velocity peak in the data. Uncertain solutions are marked in Tables 2 to 6, and should be used with caution.

Acknowledgements. We thank J. Alcolea for helpful discussions, and P. Monger for providing the FITS reader for “FG3”. We thank as well an anonymous referee for helpful comments that improved the manuscript. FC thanks the Harvard-Smithsonian Center for Astrophysics for the hospitality shown during his 18 months visit, supported by a grant of the Spanish DGICYT, which also partially supported VB under projects PB93-0048 and PB96-0104. This research has made use of the Simbad database, operated at CDS, Strasbourg, France.

References

- Brand J., Cesaroni R., Caselli P., et al., 1994, A&AS 193, 541
 Bowers P.F., Claussen M.J., Johnston K.J., 1993, AJ 105, 284
 Bowers P.F., Johnston K.J., 1994, ApJS 92, 189
 Bujarrabal V., Alcolea J., 1991, A&A 251, 536
 Cesaroni R., Palagi F., Felli M., et al., 1988, A&AS 76, 445
 Chapman J.M., Cohen R.J., 1986, MNRAS 220, 513
 Colomer F., Graham D.A., Krichbaum T.P., et al. 1992, A&A 254, L17
 Colomer F., 1996, PhD Thesis “High resolution studies of circumstellar masers”. Technical report N° 287. School of Electrical and Computer Engineering with Onsala Space Observatory, Chalmers University of Technology. Göteborg, Sweden. ISBN 91-7197-337-0.
 Colomer F., Baudry A., Graham D.A., et al. 1996, A&A 312, 950
 Cooke B., Elitzur M., 1985, ApJ 295, 175
 Danchi W.C., Bester M., Degiacomi C.G., Greenhill L.J., Townes C.H., 1994, AJ 107 (4), 1469
 Diamond P.J., Johnston K.J., Chapman J.M., et al., 1987, A&A 174, 95
 Diamond P.J., Kemball A.J., Junor W., et al., 1994, ApJ 430, L61
 Dickinson D.F., Turner B.E., Jewell P.R., Benson P.J., 1986, AJ 92, 627
 Dyck H.M., Zuckerman B., Leinert Ch., Beckwith S., 1984, ApJ 287, 801
 Engels D., Schmid-Burgk J., Walmsley C.M., 1988, A&A 191, 283
 Engels D., Winnberg A., Brand J., Walmsley C.M., 1993. In: Proc. “Astrophysical Masers” conference, A.W. Clegg and G.E. Nedoluha (Eds). Lecture Notes in Physics, Vol. 412, pp. 403. Springer-Verlag, Berlin.
 Engels D., Lewis B.M., 1996, A&AS 116, 117
 Feast M.W., Glass I.S., Whitelock P.A., Catchpole R.M., 1989, MNRAS 241, 375
 Gezari D.Y., Schmitz M., Mead J.M., 1987, “Catalog of Infrared Observations”. NASA Publication 1196.
 Goldreich P., Kwan J., 1974, ApJ 190, 27
 Greenhill L.J., Colomer F., Moran J.M., et al., 1995, ApJ 449, 365
 Imai H., Sasao T., Kameya O., et al., 1997, A&A 317, L67
 Johnston K.J., Spencer J.H., Bowers P.F., 1985, ApJ 290, 660
 Knapp G.R., Morris M., 1985, ApJ 292, 640
 Lane A.P., Johnston K.J., Bowers P.F., Spencer J.H., Diamond P.J., 1987, ApJ 323, 756
 Loup C., Forveille T., Omont A., Paul J.F., 1993, A&AS 99, 291
 Lucas R., Bujarrabal V., Guilloteau S., et al., 1992, A&A 262, 491
 Margulis M., Van Blerkom D.J., Snell R.L., Kleinmann S.G., 1990, ApJ 361, 673
 Menten K.M., Young K., 1995, ApJ 450, L67
 Nyman L-Å., Booth R.S., Carlström U., et al., 1992, A&AS 93, 121
 Press W.H., Flannery B.P., Teukolsky S.A., Vetterling W.T. (Eds): Numerical Recipes. The Art of Scientific Computing. Cambridge University Press, 1986.
 Reid M.J., Menten K.M., 1990, ApJ 360, L51
 Reid M.J., Menten K.M., 1997, ApJ 476, 327
 Sliotmaker A., Herman J., Habing H.J., 1985, A&AS 59, 465
 Spencer J.H., Johnston K.J., Moran J.M., Reid M.J., Walker R.C., 1979, ApJ 230, 449
 Sullivan W.T., 1973, ApJS 25, 393
 Walker R.C., 1984, ApJ 280, 618
 Yates J.A., Cohen R.J., 1994, MNRAS 270, 958
 Zuckerman B., Dyck H.M., 1986, ApJ 304, 394